PAPER • OPEN ACCESS

Image quality evaluation of a new high-performance ring-gantry cone-beam computed tomography imager

IOP Publishing Phys. Med. Biol. 69 (2024) 105018 https://doi.org/10.1088/1361-6560/ad3cb0

Physics in Medicine & Biology

IPEM Institute of Physics and Engineering in Medicine

OPEN ACCESS

RECEIVED
3 November 2023

REVISED
19 March 2024

ACCEPTED FOR PUBLICATION
9 April 2024

PUBLISHED
7 May 2024

PAPER

Image quality evaluation of a new high-performance ring-gantry cone-beam computed tomography imager

Didier Lustermans[1], Gabriel Paiva Fonseca[1], Vicki Trier Taasti[1], Agustinus van de Schoot[2], Steven Petit[2], Wouter van Elmpt[1] and Frank Verhaegen[1]

[1] Department of Radiation Oncology (Maastro), GROW Research Institute for Oncology and Reproduction, Maastricht University Medical Centre+, Maastricht, The Netherlands

[2] Erasmus MC Cancer Institute, University Medical Center Rotterdam, Department of Radiotherapy, Rotterdam, The Netherlands

E-mail: didier.lustermans@maastrichtuniversity.nl

Keywords: radiotherapy, image quality, cone-beam computed tomography, metal artifact reduction, extended field-of-view, CT number accuracy

Supplementary material for this article is available online

Abstract

Objective. Newer cone-beam computed tomography (CBCT) imaging systems offer reconstruction algorithms including metal artifact reduction (MAR) and extended field-of-view (eFoV) techniques to improve image quality. In this study a new CBCT imager, the new Varian HyperSight CBCT, is compared to fan-beam CT and two CBCT imagers installed in a ring-gantry and C-arm linear accelerator, respectively. *Approach*. The image quality was assessed for HyperSight CBCT which uses new hardware, including a large-size flat panel detector, and improved image reconstruction algorithms. The decrease of metal artifacts was quantified (structural similarity index measure (SSIM) and root-mean-squared error (RMSE)) when applying MAR reconstruction and iterative reconstruction for a dental and spine region using a head-and-neck phantom. The geometry and CT number accuracy of the eFoV reconstruction was evaluated outside the standard field-of-view (sFoV) on a large 3D-printed chest phantom. Phantom size dependency of CT numbers was evaluated on three cylindrical phantoms of increasing diameter. Signal-to-noise and contrast-to-noise were quantified on an abdominal phantom. *Main results*. In phantoms with streak artifacts, MAR showed comparable results for HyperSight CBCT and CT, with MAR increasing the SSIM (0.97–0.99) and decreasing the RMSE (62–55 HU) compared to iterative reconstruction without MAR. In addition, HyperSight CBCT showed better geometrical accuracy in the eFoV than CT (Jaccard Conformity Index increase of 0.02–0.03). However, the CT number accuracy outside the sFoV was lower than for CT. The maximum CT number variation between different phantom sizes was lower for the HyperSight CBCT imager (~100 HU) compared to the two other CBCT imagers (~200 HU), but not fully comparable to CT (~50 HU). *Significance*. This study demonstrated the imaging performance of the new HyperSight CBCT imager and the potential of applying this CBCT system in more advanced scenarios by comparing the quality against fan-beam CT.

1. Introduction

One of the important developments in radiotherapy is the integration of kV x-ray imaging panels into radiotherapy treatment machines to enable image-guided radiotherapy (IGRT) and online adaptive radiotherapy. Imaging panels in cone-beam computed tomography (CBCT) have significantly enhanced treatment accuracy by enabling accurate positioning and setup as well as improving the overall effectiveness of the treatment (Jaffray *et al* 2002, Hofmaier *et al* 2017, Cai *et al* 2019). Despite its benefits for IGRT, currently in most situations on-board CBCT is not suitable for plan adaptation due to limited field-of-view (FoV) and

suboptimal image quality for delineation (e.g. caused by photon scatter) compared to fan-beam computed tomography (CT) (Jin *et al* 2010, Lim *et al* 2022).

Commonly, CBCT reconstruction is performed using a filtered back projection with the Feldkamp–Davis–Kress (FDK) algorithm (Lim *et al* 2022). However, this method has been shown to handle image noise and artifacts insufficiently, which could lead to larger variations in CT numbers compared to CT images (Hatton *et al* 2009, Lim *et al* 2022). A study showed this is dependent on the CBCT imaging system, with some imagers having performances closer to CT (De Smet *et al* 2016). Recently, iterative reconstruction (IR) algorithms have been developed for CBCT imagers to improve the image quality. Multiple studies have evaluated IR compared to FDK reconstruction and demonstrated better CT number accuracy, higher contrast-to-noise (CNR), and reduction in image noise (Cai *et al* 2019, Gardner *et al* 2019, Jarema and Aland 2019, Lim *et al* 2022, Henke *et al* 2023). However, less is known about the CBCT quality in more challenging scenarios, such as metal implants, data outside the standard FoV (sFoV) and visualization of patient anatomy outside the standard reconstruction diameter of the CBCT acquisition. In most modern CT scanners, this is accounted for by integrated metal artifact reduction (MAR) (Puvanasunthararajah *et al* 2021) and extended FoV (eFoV) methods (Cheung *et al* 2019, Fonseca *et al* 2021).

Recently, developments in CBCT imagers (HyperSight imager, Varian Medical Systems, a Siemens Healthineers Company) allowed to improve CBCT acquisition and image quality. The imager includes increased flat panel dimensions and improvements in image processing algorithms. This imager offers eFoV (up to 70 cm), CBCT MAR, and decreased acquisition time (5.9 s) to counteract the effect of patient motion. The implementation of such new imagers and the added features could enhance the radiotherapy workflow, also for on-line and off-line adaptive radiotherapy workflows. However, a thorough assessment of the image quality of these advanced features is crucial before integrating the workflows into clinical practice.

Therefore, this study aimed to assess the image quality of the HyperSight imager in terms of MAR, eFoV, phantom size dependency of CT numbers, signal-to-noise (SNR) and CNR, using commercially available and in-house phantoms. The results were compared to standard CT, and CBCT of a previous version of the ring-gantry imager and a C-arm linear accelerator (linac), to enable an extensive evaluation of the available imagers and the added value of HyperSight CBCT.

2. Material and methods

2.1. Imagers

Image acquisitions were performed with a HyperSight CBCT imager, integrated in a Halcyon ring-gantry treatment machine (v4.0, Varian Medical Systems). This bore-enclosed CBCT imager included a large flat panel detector (86 × 43 cm^2; panel in center position), that featured a cesium iodine scintillator (Robar *et al* 2023). The detector used an anti-scatter grid with a 15:1 aspect ratio and 44 lamellae/cm, and allowed a pixel-size of 0.28 mm and image readout up to 70 frames per second. Data acquisition with this panel occurred in full-fan mode and enabled a scan reconstruction diameter of 53.8 cm, as well as advanced software for CBCT IR. The software incorporated advanced subject scatter corrections using the Acuros® based scatter model (Maslowski *et al* 2018) and object scatter removal through implementation of Monte-Carlo based hardware scatter correction. In addition, it uses MAR and eFoV techniques (up to 70 cm diameter) to enhance image quality. The imager had a specific CBCT for Planning mode (CBCTp mode) intended for acquisition of images which could be used for radiotherapy treatment planning. CBCTp allowed for acquisition of a topogram and more flexibility to vary the imaging parameters, and thereby to design target group specific imaging protocols. Additionally, it can scan with higher dose levels and enabled MAR and eFoV reconstruction to increase the image quality. In this study, the CBCTp mode was used for all HyperSight image acquisitions.

The performance of the HyperSight imager was compared to a CT scanner (SOMATOM Definition Drive, Siemens Healthineers, Forchheim, Germany), and two CBCT imaging systems. One CBCT system was of an earlier model ring-gantry linac (Ethos v3.1; Varian Medical Systems) that was not equipped with the HyperSight imager, and this will be referred to as Regular CBCT. This term is chosen as it has the 'standard' functions of the system without the inclusion of the HyperSight imager, but this does not mean it is the regularly used scanner in every clinic. The second CBCT system in the comparison was a CBCT imaging system of a C-arm linac (TrueBeam v2.7; Varian Medical Systems), which will be called TrueBeam CBCT throughout the study. The imager of the Regular CBCT used the same anti-scatter grid as the HyperSight CBCT, but this CBCT had a smaller panel detector size (43 × 43 cm^2), it had no possibility for CBCTp mode, and it lacked features such as MAR and eFoV. Whereas, the HyperSight CBCT always applied a full-fan acquisition with one fixed bowtie filter for both smaller and larger diameter anatomies, the Regular CBCT always applied a half-fan configuration, again using only one fixed bowtie filter intended for all anatomies. The TrueBeam CBCT imager (40 × 30 cm^2, pixel size of 0.388 mm) contained an anti-scatter grid of 10:1 aspect ratio with 60 lamellae/cm and different bowtie

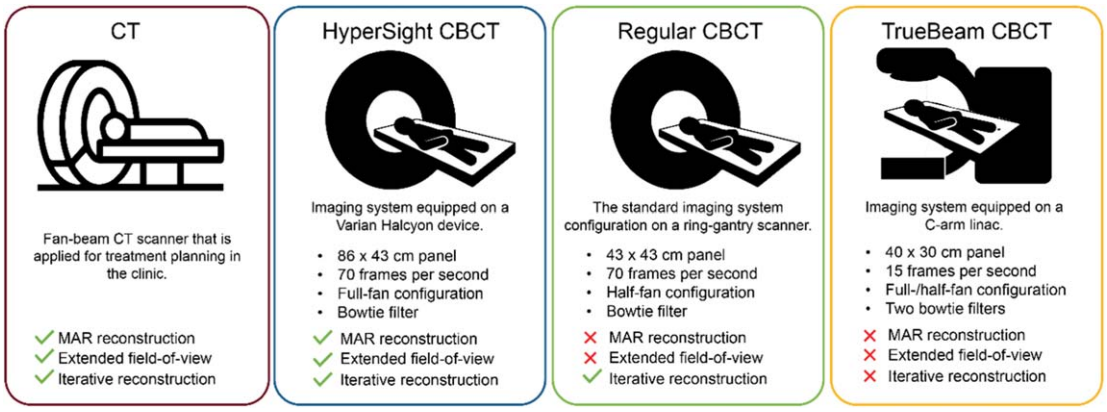

Figure 1. Schematic representation of the four evaluated scanners in this study, CT, HyperSight CBCT, Regular CBCT and TrueBeam CBCT with their corresponding specifications.

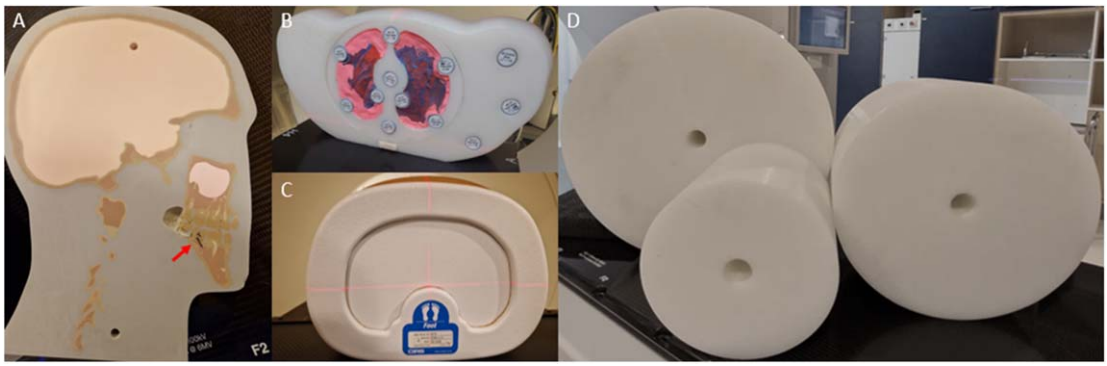

Figure 2. The four different phantoms used in this study to evaluate the performance of the HyperSight CBCT imager. (A) CIRS Proton Therapy Dosimetry Head phantom with a metal spine implant (not visible) and a metal tooth implant (red arrow), used to assess the metal artifact reduction feature. *Size*: 18 × 22 × 27 cm. (B) In-house 3D-printed chest phantom, used to evaluate the extended field-of-view. *Size*: 27 × 9 × 56 cm. (C) CIRS Triple Modality 3D Abdominal Phantom, used to calculate the image quality in terms of noise, SNR and CNR. *Size*: 26 × 12.5 × 19 cm. (D) Three high-density polyethylene (HDPE) phantoms (20, 30, and 40 cm in diameter); these had a hole in the center of the phantoms for insertion of tissue-equivalent inserts to analyze the CT number dependency on phantom size.

filters for half- and full-fan acquisitions. Additionally, the TrueBeam CBCT did not contain MAR and eFoV and it only offered FDK reconstruction in the current machine in our clinic. Figure 1 in the demonstrates the differences in design and software in more detail.

2.2. Phantoms

For the evaluations performed in this study, four phantoms were used: three anthropomorphic phantoms (head, chest and abdomen) and cylindrical phantoms of varying size (see figure 2). The anthropomorphic phantoms include a head phantom (Proton Therapy Dosimetry Head, model 731-HN, CIRS, Sun Nuclear, Norfolk, VA, USA) to evaluate the MAR reconstruction (figure 2(A)), an in-house 3D-printed chest phantom (Fonseca *et al* 2021), with dimensions of 27 × 9 × 56 cm (height × length × width) to evaluate the eFoV (figure 2(B)), and an anthropomorphic abdomen phantom (Triple Modality 3D Abdominal Phantom, model 057A, CIRS, Sun Nuclear, Norfolk, VA, USA) to quantify noise and image quality (figure 2(C)). Three cylindrical phantoms of varying sizes (20 cm, 30 cm and 40 cm; figure 2(D)), representing typical head and abdomen sizes, were applied to assess the CT number difference between various sizes. More details about the phantom can be found in the Supplementary Material.

2.3. Image acquisitions

The scan parameters for the acquisitions of the different phantoms and each scanner can be found in tables 1–4; for each scanner, the clinical protocols were used. The HyperSight CBCT acquisitions were performed with a tube voltage of 125 kVp and a scan duration of 5.9 s or 60 s (with longer scan time only if higher dose levels for

Table 1. Scan parameters for the CT and CBCT acquisitions for the assessment of the metal artifact reduction (MAR). Not all parameter settings were available on all CBCT imagers, whereby some settings differ between the individual imagers. The phantom scanned for the evaluation is listed with some information why it is relevant. A slice thickness of 1 mm was not possible in the regular CBCT and truebeam CBCT, and for these two CBCT systems, MAR was not available (n/a).

(CB)CT imagers	CT	HyperSight CBCT	Regular CBCT	TrueBeam CBCT
Image quality with metal artifacts				
Phantom	CIRS proton therapy dosimetry head phantom (figure 2(A))			
	Includes metal spine implant and a removable tooth with a tungsten dental filling			
Field-of-view [mm]	281	281	492	465
Slice thickness [mm]	1	1	2	3
Pixel size [mm]	0.68	0.55	0.96	0.91
$CTDI_{vol}$ [mGy]	40	41	32	32
MAR applied	Yes	Yes	n/a	n/a

Table 2. Scan parameters for the CT and CBCT acquisitions for the assessment of the extended field-of-view (eFoV). eFoV was not available in the Regular CBCT and TrueBeam CBCT, these systems were therefore not included in this evaluation.

(CB)CT imagers	CT	HyperSight CBCT	Regular CBCT	TrueBeam CBCT
	Extended field-of-view			
Phantom	3D-printed chest phantom (figure 2(B))			
	The phantom size (56 cm width) is larger than the standard field-of-view (50 cm CT, 53.8 cm HyperSight CBCT)			
Field-of-view [mm]	700	700	Not included/available	
Slice thickness [mm]	1	1		
Pixel spacing [mm]	1.37	1.37		
$CDTI_{vol}$ [mGy]	20	12		

Note the maximum FoV size of 700 mm FoV was chosen to fit the phantom even with increasing the table height.

Table 3. Scan parameters for the CT and CBCT acquisitions for the assessment of the phantom size dependency of CT numbers. Not all parameter settings were available on all CBCT imagers, whereby some settings differ between the individual imagers. a slice thickness of 3 mm was not possible in the regular CBCT.

(CB)CT imagers	CT	HyperSight CBCT	Regular CBCT	TrueBeam CBCT
	Phantom size dependency of CT numbers			
Phantom	High-density polyethylene (HDPE) phantoms (figure 2(D))			
	The phantoms had different diameters (20, 30 and 40 cm), and each phantom fits tissue-equivalent rods in the iso-center			
Field-of-view [mm]	500	500	492	465
Slice thickness [mm]	3	3	2	3
Pixel spacing [mm]	0.97	0.97	0.96	0.91
$CDTI_{vol}$ [mGy]	1.5/4.5/16	20/26/52	18/18	18/18/18

Note Only the 20 cm and 30 cm diameter phantoms were evaluated for the Regular CBCT. The dose levels for all imagers were chosen to limit the noise in the acquisition based on imager specific possibility.

Table 4. Scan parameters for the CT and CBCT acquisitions for the assessment of the image noise. Not all parameter settings were available on all CBCT imagers, whereby some settings differ between the individual imagers. A slice thickness of 1 mm was not possible in the regular CBCT and truebeam CBCT.

(CB)CT imagers	CT	HyperSight CBCT	Regular CBCT	TrueBeam CBCT
	Noise, signal-to-noise and contrast-to-noise			
Phantom	Triple modality 3D abdominal phantom (figure 2(C))			
	This phantom represents the abdomen with bone and various soft tissue-equivalent organs			
Field-of-view [mm]	500	500	492	465
Slice thickness [mm]	1	1	2	3
Pixel spacing [mm]	0.97	0.97	0.96	0.91
$CDTI_{vol}$ [mGy]	20	19	21	20

reduced noise levels were needed, i.e. for the largest cylindrical phantom). For the chest phantom (which had a length of 9 cm), the beam was collimated in the scan direction to only cover the phantom to limit scatter.

The CT scans were acquired at 120 kVp, a pitch of 0.9, and collimation width of 64 × 0.6 mm. For the Regular CBCT and TrueBeam CBCT imagers, the scan parameters could not be chosen as freely as for the HyperSight CBCT and the CT and no collimation in the scan direction could be performed. The Regular CBCT had a scan time of 30 s and a tube voltage of 125 kVp, while the TrueBeam CBCT had a scan time of 60 s and tube voltage of 100 kVp (used for the scanning of the head phantom) and 125 kVp (used for the other phantoms).

2.4. Image quality evaluations

2.4.1. Metal artifact reduction

The anthropomorphic phantom used to evaluate MAR reconstruction contained tissue-equivalent tissues, but most importantly a removable tooth where either a tooth implant containing tungsten (tooth T) or a standard tooth not containing metal (tooth S) can be inserted. Furthermore, the phantom contains a non-replaceable titanium spine prosthesis.

The metal artefacts caused by the tungsten tooth and the titanium spine prosthesis were evaluated separately, denoted dental evaluation and spine prosthesis evaluation (figure S1A in supplementary material). In the dental evaluation, two phantom setups were used, one with tooth S inserted (setup 1) and one with tooth T inserted (setup 2). These two setups were scanned with the CT and HyperSight CBCT, and two different reconstructions, normal IR and iterative MAR. The Regular CBCT and TrueBeam CBCT imagers used in this study did not include any MAR features, and therefore only IR or FDK reconstruction was used, respectively. The scan of setup 1 reconstructed with IR was used as reference image, as this setup did not contain metal artifacts in the dental region (for TrueBeam CBCT, the FDK reconstruction of setup 1 was seen as the reference). This was compared to the scan of setup 2 reconstructed with MAR (HyperSight CBCT and CT) and without MAR (all (CB)CT imagers) by evaluating a square region-of-interest (ROI) of 9 cm^3 including 3 axial slices. The ROI was placed in the soft tissue adjacent to the tooth implant (figure S1B in supplementary material). For the spine prosthesis evaluation, the analysis was performed based on a square ROI (3 sagittal slices) of 18 cm^3 around the metal prosthesis containing both soft tissue and bone (figure S1B in supplementary material). Because the spine prosthesis could not be removed only setup 1 was used, and MAR reconstruction in setup 1 was used as reference and compared to IR reconstruction without MAR (HyperSight CBCT and CT).

These setups were compared quantitatively by the structural similarity index measure (SSIM) (Wang *et al* 2003, 2004) given by equation (1):

$$\mathrm{SSIM} = l(x,\ y)^{\alpha} * c(x,\ y)^{\beta} * s(x,\ y)^{\gamma} \tag{1}$$

with $l(x,\ y)$ is the luminance, $c(x,\ y)$ is the contrast and $s(x,\ y)$ is the structure, see the Supplementary Material for a detailed description (Wang *et al* 2004). The SSIM provides an indication of the image quality, by comparing the reference image (metal free image) and the analyzed image for distortions, resulting in a similarity value (perfect similarity = 1, with small variations demonstrating clinical importance (Joemai and Geleijns 2017)). The SSIM value is given at pixel-level, and the mean ± standard deviation (SD) was quantified for the volumetric ROI. A schematic of the evaluation process and the placement of the evaluated ROIs are shown in figure S1 in the supplementary material.

Additionally, the Root-mean-squared error (RMSE) was quantified by calculating the difference in CT numbers (given in Hounsfield unit (HU)) within the ROI volume between the two setups, as given in equation (2):

$$\mathrm{RMSE} = \sqrt{\frac{\sum_i^N (x_i - y_i)^2}{N}}, \tag{2}$$

where x_i, y_i and N are the pixel value in image x, pixel value in image y, and the number of pixels, respectively.

2.4.2. Extended field-of-view (eFoV)

The commercially available phantoms in our clinic (dimension < 50 cm) all fitted within the sFoV of the HyperSight CBCT (53.8 cm) and CT scanner (50 cm), therefore the evaluation of the eFoV was carried out on an in-house 3D-printed chest phantom (Fonseca *et al* 2021), with dimensions of 27 × 9 × 56 cm (height × length × width) that included several holes for the insertion of cylindrical tissue-equivalent inserts of the Gammex Advanced Electron Density phantom (Model 1472; Sun Nuclear, Middleton, WI, USA).

The Regular CBCT and TrueBeam CBCT imagers used in this study did not have a reconstruction option including eFoV, therefore this assessment only included acquisitions performed with the HyperSight CBCT and CT imagers. The evaluation was divided into an assessment of the CT number accuracy and the geometrical accuracy (Fonseca *et al* 2021). For the geometrical accuracy, images were acquired by increasing the table height by 2 cm increments (five times) to vary the volume of the phantom in the eFoV (outside the standard FoV). The

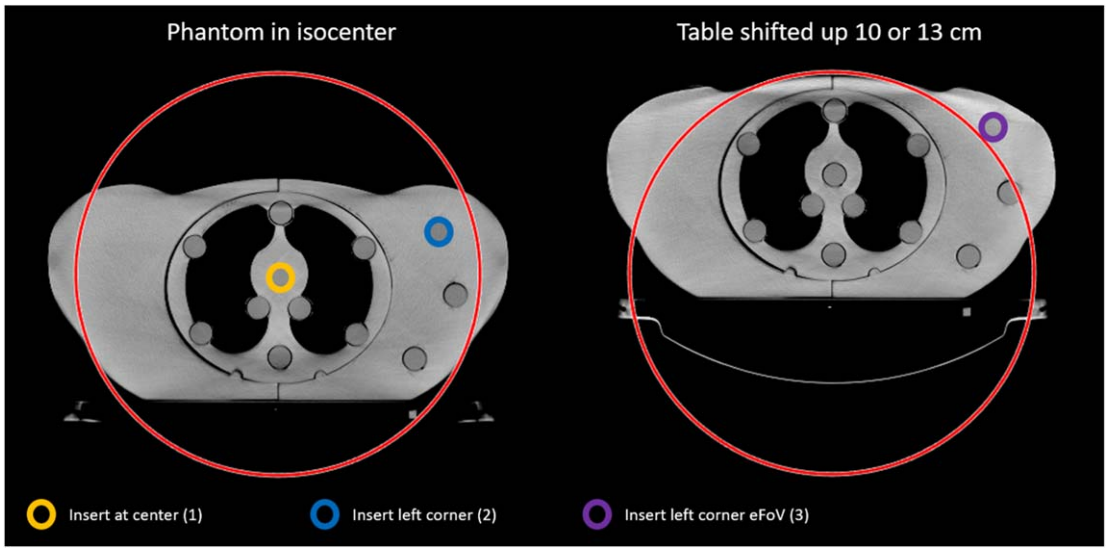

Figure 3. Visualization of the insert position for the CT number accuracy evaluation of the extended field-of-view (eFoV). It shows the two different table heights with the standard FoV (sFoV) marked with a red circle and indicates from which insert positions the mean and standard deviation of the CT numbers were calculated: (1) insert in the isocenter, (2) insert in the top left corner but still inside the sFoV, or (3) the insert in the top left corner (3) but in the eFoV.

accuracy was evaluated after rigid registration of the images acquired with the varying table heights to a reference image. The reference image was acquired from a different CT imager (Siemens Go.Open Pro CT scanner), as this scanner has a larger standard FoV of 60 cm which fully covers the chest phantom when placed at the isocenter. The acquisition settings were kept the same as for the other systems. Binary masks were created from all images (threshold at −600 HU, manual visualization), with voxel values of 1 inside the phantom and 0 outside (it was visually ensured that this thresholding excluded the CT/treatment table from the mask). The Jaccard Conformity Index (dividing the intersect of two regions by the union of these regions; see equation S6 in the supplementary material) (Real and Vargas 1996) was used to quantitatively evaluate the overlap between the regions inside the phantom in the evaluated and reference image. A Jaccard Conformity Index of 1 indicates a perfect match between the regions. The computation excluded the sFoV region and focused solely on the phantom areas within the eFoV region (Fonseca *et al* 2021).

The CT number accuracy assessment was performed by placing the tissue-equivalent inserts in three positions: (1) isocenter of the phantom (table height: 0 cm moved from isocenter), (2) at the top left corner of the phantom (table height: 0 cm moved), and (3) at the top left corner of the phantom with the table height increased by 13 cm for HyperSight CBCT and by 10 cm for CT due to bore restrictions (see figure 3). The CT number accuracy was defined as the difference between the mean CT number for the insert placed in the isocenter and placed close to the edge (position 1 versus 2) and placed outside the sFoV (position 1 versus 3) (Fonseca *et al* 2021).

2.4.3. Phantom size dependency of CT numbers

Three cylindrical phantoms (figure 2(D)) of HDPE were used to evaluate the accuracy and the dependency of the CT numbers for various body sizes. Tissue-equivalent inserts of the Gammex phantom were inserted in the cylindrical hole at the center of the HDPE phantoms. The tissue-equivalent inserts had a diameter of 28 mm and included high-equivalency (HE) adipose tissue, HE solid water, HE Liver, HE Inner Bone, $CaCO_3$ 30%, $CaCO_3$ 50%, and HE Cortical Bone.

The dose levels for the (CB)CT imagers were chosen to keep the noise levels similar for the three phantom sizes (not fully possible due to restrictions on dose levels). Increasing the dose above local clinical practice (as used in clinical protocols) would mostly affect the SD and less the mean. The mean and SD of the CT numbers were extracted in a central ROI (diameter = 15.6 mm, number of slices = 9, slice thickness = 3 mm) in the seven tissue-equivalent inserts for all (CB)CT imagers. Due to time constraints, for the Regular CBCT, only a selection of phantom sizes (20 cm and 30 cm) and inserts (HE adipose tissue, HE solid water, HE Liver, HE Inner Bone, HE Cortical Bone) were used. The phantom size dependency of CT numbers was visualized by plotting the differences between the mean CT number for the 20 cm phantom (used as reference) and the 30 cm or 40 cm phantom for each insert.

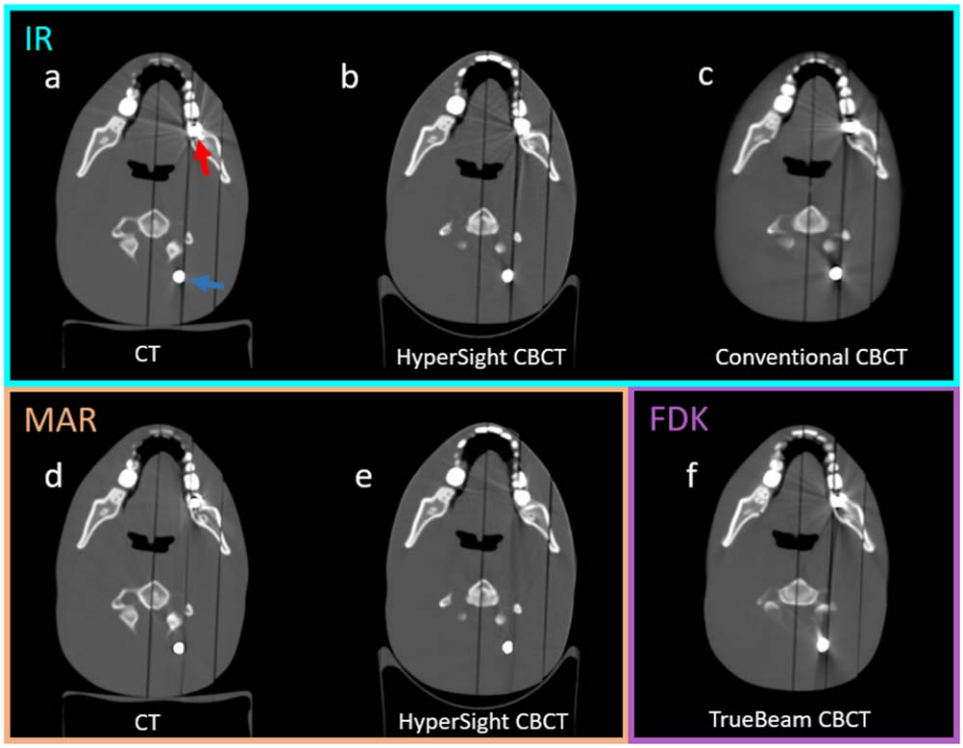

Figure 4 Visualization of an axial slice containing metal artifacts arising from tooth T (red arrow) and spine implant (blue arrow) after reconstruction with iterative reconstruction (IR) for (a) CT, (b) HyperSight CBCT, and (c) Regular CBCT. In addition, it shows metal artifact reduction (MAR) reconstruction for (d) CT and (e) HyperSight CBCT, and FDK reconstruction for (f) TrueBeam CBCT. A more detailed version of the artifacts around the dental implant and spine implant can be found in figure S2 in the supplementary material. A window level setting of [−700, 1000] was used for all images.

2.4.4. Image noise, SNR and CNR

The CT image noise (defined as the SD), SNR and CNR were evaluated using an abdomen phantom (figure 2(C)) that contained multiple tissues such as kidney, liver and bone.

For the image acquisition for all (CB)CT imagers, the phantom was placed at the isocenter. The CT image quality parameters were evaluated in the kidney, liver and spine. At first, consistency throughout the image was evaluated in identical soft tissue by extracting the mean CT number and SD in three cylindrical ROIs, with a volume of 6.8 cm^3 (9 slices), placed next to each other (figure 8, orange circles). Additionally, a line profile was extracted in the horizontal direction that crossed these three ROIs (figure 8). Secondly, the SNR and CNR were extracted as:

$$\mathrm{SNR} = \frac{\mathrm{mean\ \ ROI}}{\sqrt{(\mathrm{SD\ \ ref}^2 + \mathrm{SD\ \ ROI}^2)}} \tag{3}$$

$$\mathrm{CNR} = \frac{\mathrm{mean\ \ ROI} - \mathrm{mean\ \ ref}}{\sqrt{(\mathrm{SD\ \ ref}^2 + \mathrm{SD\ \ ROI}^2)}}. \tag{4}$$

Here mean ROI and mean ref are the mean CT number of the investigated ROI (kidney, liver, or spine) and the reference ROI (soft tissue), respectively, while SD ROI and SD ref are the SD of the CT numbers in these ROIs (see figure S4 in Supplementary Material for the placement). Both the SNR and equations (equations (3) and (4)) are normalized regarding the noise by combining the SD of a soft tissue reference ROI and the evaluated ROI.

3. Results

3.1. Metal artifact reduction

Figure 4 visualizes axial images for all the imagers with their possible reconstruction algorithms. For the dental evaluation, an individual reference image that did not contain metal artifacts (setup 1; tooth S inserted) was acquired for each individual (CB)CT imager and compared to an image with metal artifacts (setup 2; tooth T inserted) that was reconstructed with and without MAR reconstruction. The SSIM quantification demonstrated an increase in similarity between setup 1 and setup 2 when utilizing the iterative MAR reconstruction algorithms available for the CT and HyperSight CBCT imagers compared to reconstruction without MAR. The increase in

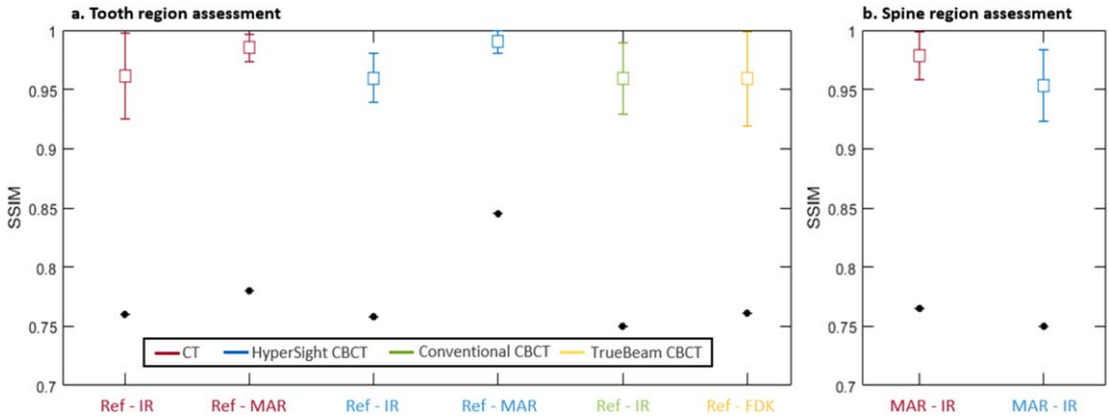

Figure 5. (a) Mean ± SD of the structural similarity index measure (SSIM) for the dental evaluation by quantifying it in the axial ROI (figure S1B) on the CT (red), HyperSight CBCT (blue), Regular CBCT (green), and TrueBeam CBCT (yellow). In addition, the highest outlier (black dot) are shown for every system. Two comparisons were performed for CT and HyperSight CBCT, the reference image (Ref; setup 1, tooth S inserted) reconstructed with iterative reconstruction (IR) against setup 2 (tungsten tooth inserted) with either metal artefact reduction (MAR) reconstruction or IR. For the Regular CBCT and TrueBeam CBCT, which did not include MAR, only one dental evaluation was performed, setup 1 versus 2 both with IR for Regular CBCT or both with Feldkamp–Davis–Kress (FDK) reconstruction for TrueBeam CBCT. (b) Mean ± SD of the SSIM for the spine evaluation quantified in a sagittal ROI (Figure S1B). Only CT and HyperSight CBCT were included, since here the reference image was setup 1 with MAR reconstruction which was compared to setup with IR. Note, different ROIs were used in the dental and spine evaluation, even though the same images were used for the two evaluations.

SSIM, calculated in the dental ROI (Figure S1B), is seen by the higher mean value and lower SD for the MAR reconstruction (figure 5(a)). It improved the mean SSIM in the ROI from 0.96 to 0.99 for HyperSight CBCT and from 0.96 to 0.98 for CT (table S1 in supplementary material) compared to IR without MAR. In addition, using MAR decreased the RMSE by 7 HU (from 62 to 55 HU) and 18 HU (from 110 to 92 HU) for HyperSight CBCT and CT, respectively. For the Regular CBCT and TrueBeam CBCT, which had no MAR reconstruction, the SSIM was 0.96 for both imagers, and the RMSE was 133 HU and 86 HU, respectively.

The head phantom contained in addition a spine prosthesis (figure 4; blue arrow). The spine evaluation contained a comparison between the MAR reconstruction and the IR without MAR, as the spine was not replaceable and thus an artifact free reference image was not possible. The SSIM in the titanium spine prosthesis ROI (see figure S1B in the supplementary material) was 0.95 ± 0.03 (figure 5(b)) for HyperSight CBCT and was lower than the SSIM of 0.98 ± 0.02 seen for the CT imager. The RMSE CT number difference between a MAR reconstruction and IR reconstruction was also worse for HyperSight CBCT (147 HU) compared to CT (66 HU) in the specified ROI.

3.2. Extended field-of-view

Figure 6(A) shows qualitatively the body contour differences in volume by purple (increase in volume compared to reference) or green (decrease in volume compared to reference) color in the eFoV between the ground truth (Go.Open Pro, full phantom inside sFoV) and the image of the CT or HyperSight CBCT, with some part of the phantom in the eFoV. The differences were shown for different phantom volumes outside the sFoV (when increasing the table height, a larger volume of the phantom was in the eFoV) and were quantified with the Jaccard Conformity Index (calculated separately for the left and right side of the phantom that falls outside the sFoV; figure 6(B)). The overlap accuracy differed per table height (phantom volume outside sFoV) and showed a Jaccard Conformity Index range from 0.80 to 0.96. The evaluated volumes for CT were higher, due to a smaller sFoV (50 cm for CT and 53.8 cm for HyperSight CBCT). Figure 6(B) shows that HyperSight CBCT in general had a higher Jaccard Conformity Index than CT for similar phantom volumes outside the sFoV. Both imagers demonstrated an overestimation of the volume compared to the reference (figure 6(A), purple region).

The CT number accuracy evaluation showed the opposite tendency, since here HyperSight CBCT had larger CT number differences than CT when comparing the CT numbers of individual tissue-equivalent inserts placed in the isocenter (position 1, reference) and in the eFoV (position 3). However, both imagers mostly underestimated the CT numbers for the inserts in position 3. The maximum difference was found for HE cortical bone in both imagers with differences up to 421 HU (CT) and 470 HU (HyperSight CBCT) as seen in figure 6(C).

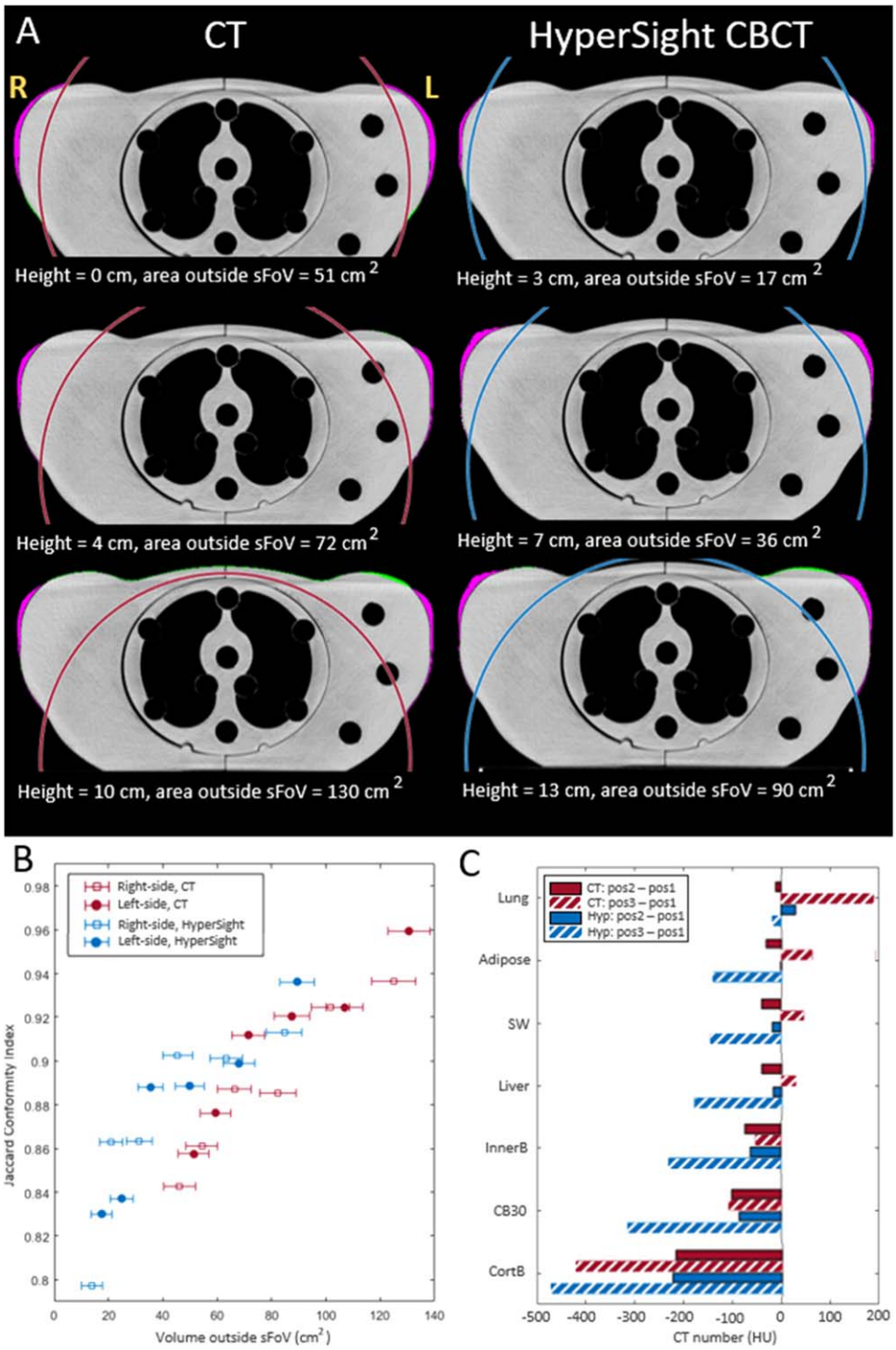

Figure 6. (A) Images acquired with CT and HyperSight CBCT with varying phantom volumes in the extended field-of-view (eFoV) compared to the reference image (acquired on the Siemens Go. Open Pro, with full phantom volume inside the standard FoV (sFoV)). Purple areas indicate an increase in volume compared to the reference image, while green indicates a decrease in volume compared to the reference image. The red (CT) and blue (HyperSight CBCT) circle (partly shown) indicates the sFoV (50 cm for CT and 53.8 cm for HyperSight CBCT). Different heights are shown between the two scanners, to ensure the volume outside the sFoV was more comparable for the two systems, as the scanners have different sFoV sizes. (B) Jaccard Conformity Index for the right and left breast (indicated by the yellow R and L in top left corner of (A) for various volumes of the phantom in the eFoV. C) CT number differences between the inserts placed in the isocenter (pos 1) and placed in the top left corner with table height of 0 cm (pos2; solid bars) or in the top left corner with table height at 13 cm (HyperSight CBCT) and 10 cm (CT), whereby the insert was in the eFoV (pos3; hashed bars) for multiple tissue-equivalent phantom inserts (for insert positions, see figure 3). *Note:* Due to a narrower bore for the CT, the maximum table height increase for CT was 10 cm, while it was 13 cm for HyperSight CBCT. However, the smaller diameter of the sFoV for CT, larger volumes of the phantom were in the eFoV. *Abbreviations:* Lung—Lung LN450, Adipose—HE adipose, SW—HE solid water, Liver—HE liver, InnerB—HE inner bone, CB30—$CaCO_3$ 30%, CortB—HE cortical bone.

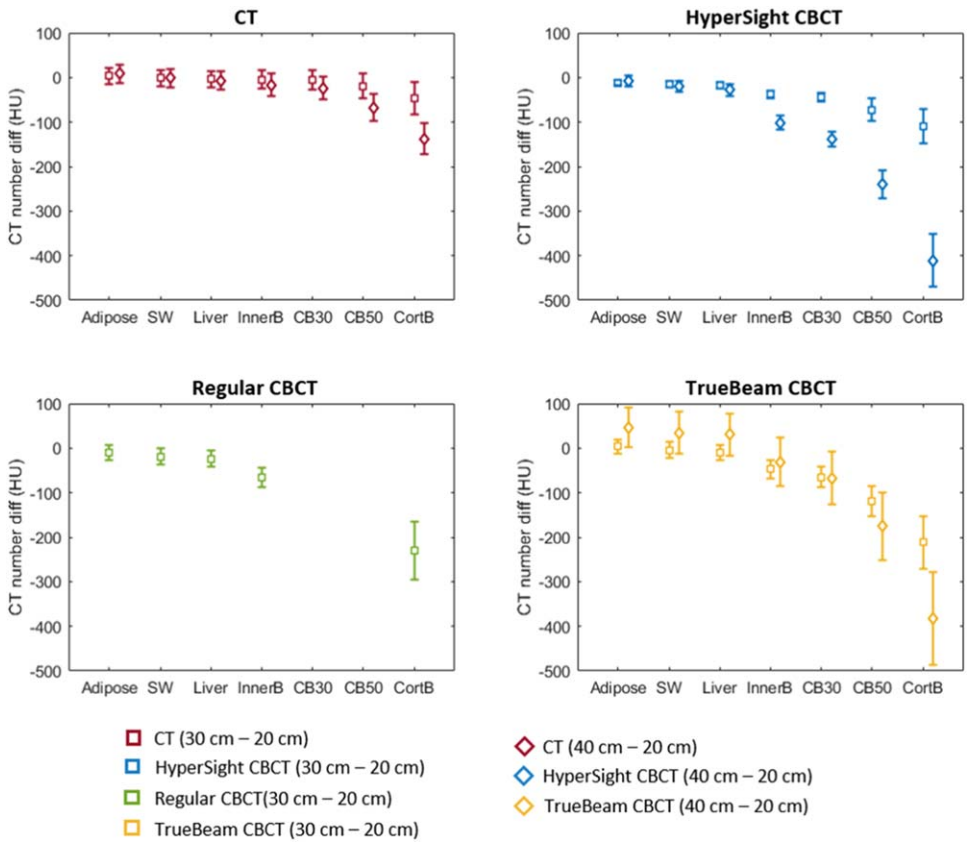

Figure 7. CT number size dependency for CT (red), HyperSight CBCT (blue), Regular CBCT (green), and TrueBeam CBCT (yellow). It shows the differences in mean CT numbers between the 20 cm and 30 cm phantom (squares) and between the 20 cm and 40 cm phantom (diamonds). *Abbreviations:* Adipose—HE adipose, SW—HE solid water, Liver—HE liver, InnerB—HE inner bone, CB30—$CaCO_3$ 30%, CB50—$CaCO_3$ 50%, CortB—HE cortical bone. *Note:* For the Regular CBCT, no measurements were performed for the 40 cm phantom and for the $CaCO_3$ 30% and $CaCO_3$ 50% inserts.

3.3. Phantom size dependency of CT numbers

The mean ± SD CT number of the tissue-equivalent inserts are shown in figure S3 in Supplementary Material for all (CB)CT imagers. The differences in CT numbers between the 20 cm phantom and the 30 or 40 cm phantom are shown in figure 7. A larger decrease in the mean CT number, especially for high-density bone materials, was seen for HyperSight CBCT compared to CT, e.g. the CT number difference for HE Cortical bone between the 20 and 40 cm phantom was 138 HU for CT and 413 HU for HyperSight CBCT. However, the CT number difference between the 20 cm and 30 cm phantom for Regular CBCT and TrueBeam CBCT showed higher differences compared to HyperSight CBCT, with even a slight increase (difference >0 HU) in soft tissue CT number for the TrueBeam CBCT between the 20 cm and 40 cm phantom, for all other imagers the three soft tissue inserts had absolute CT number difference below 28 HU.

3.4. Image noise, SNR and CNR

Figure 8(A) shows axial images of the Triple Modality 3D Abdominal Phantom containing various structures such as liver and kidney, as well as the position of the CT number line profiles for all (CB)CT imagers. The CT number line profiles showed fewer discrepancies between HyperSight CBCT and CT than between Regular CBCT and TrueBeam CBCT and CT (figure 8(B)). Moreover, the presence of cupping artifacts were seen in the Regular CBCT and TrueBeam CBCT. The image quality was additionally quantified for the (CB)CT imagers by extracting mean ± SD in three cylindrical ROIs (orange circles) next to each other in the soft tissue region (figure 8(C) and table S2 in supplementary material). These results demonstrated consistency for HyperSight CBCT (mean 26 ± 9 HU) and for CT (mean 39 ± 14 HU) between the three ROIs with low SDs. More variation was seen for Regular CBCT and TrueBeam CBCT (60 ± 16 HU and 32 ± 29 HU, respectively); also note that for both systems, one ROI had a much lower mean CT number compared to the two other ROIs (figure 8(C)).

The SNR and CNR demonstrated limited differences between HyperSight CBCT and CT, with a slight increase for the HyperSight CBCT images (Table S3 in Supplementary Material). Additionally, noise levels (quantified by SD) were similar for HyperSight CBCT and CT. Compared to Regular CBCT, HyperSight CBCT demonstrated an increase in kidney SNR (4.1 (Regular CBCT) versus 6.7 (HyperSight CBCT)) and CNR (1.9

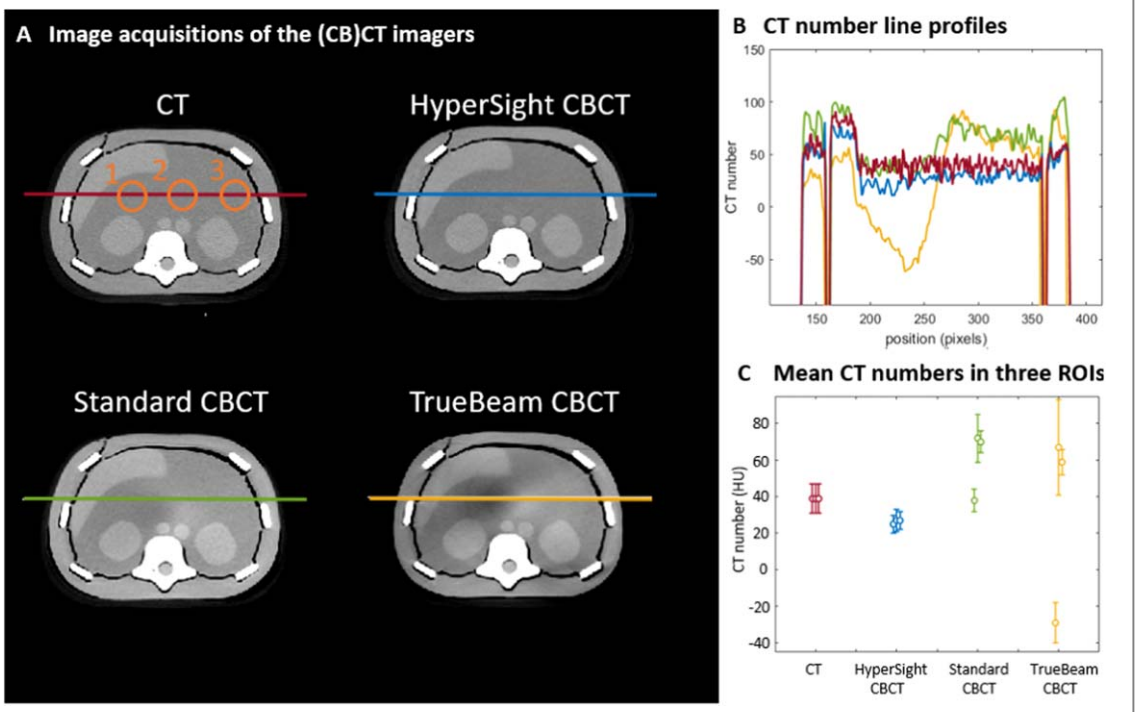

Figure 8 (A) Axial slice images acquired on each (CB)CT imager (CT, HyperSight CBCT, Regular CBCT, TrueBeam CBCT) with an indication of the position of the CT number line profile (colored lines) and the three ROIs in soft tissue (orange circles on CT). Window level setting [−180, 220] in all four images. (B) The CT number line profiles for all the imagers, encompassing liver and soft tissue. (C) Plot of the mean and SD CT numbers for the three ROIs (orange circles) in all (CB)CT imagers.

versus 3.9) and lower noise levels of 7.4 HU (HyperSight CBCT) compared to 19.4 HU (Regular CBCT; table S3 in Supplementary Material).

4. Discussion

This study assessed the novel features of the HyperSight CBCT imager by evaluating the image quality in terms of MAR, eFoV, phantom size dependency of CT number, and image quality in various phantoms compared to other commercial (CB)CT imagers. To the best of our knowledge, this is the first study of the image quality performance for the HyperSight CBCT imager, and such evaluation is crucial before integration of these advanced features in the clinical workflow. The study showed MAR reconstruction comparable to CT (figures 4 and 5), and HyperSight CBCT had a better geometrical accuracy in the eFoV than CT (quantified by the Jaccard Conformity Index), but a lower CT number accuracy (figure 6). HyperSight CBCT also demonstrated comparable CT number line profiles with CT, whereas a larger difference was seen between CT and the predecessor CBCT imagers (figure 8).

The performance of IR has been investigated in various studies and compared to FDK reconstruction (Cai *et al* 2019, Gardner *et al* 2019, Jarema and Aland 2019, Lim *et al* 2022), and IR has even been demonstrated to decrease metal artifacts (Washio et al 2020). It has also been shown that megavolt imaging had preference over kV imaging in terms of reducing metal artifact (Harris *et al* 2023). However, commercial MAR reconstruction algorithms in CBCT imagers have not been available until now. In this study, the MAR evaluations were performed on an anthropomorphic head phantom which consisted of four slabs cut in the sagittal direction which allowed the user to remove a tooth and replace it with a tungsten version. However, the resulting air gaps between the individual slabs were not fully reproducible, and the geometry of the phantom could differ slightly between the different image acquisitions after replacing the tooth insert. It was chosen to use rigid registration and not to apply other algorithms, such as deformable image registration, as such algorithms could modify the structures and artifacts. In figure 4 it is visible that the MAR algorithm in both CT and HyperSight CBCT smoothen the air gap between individual slabs, as the MAR algorithm expects the large differences in CT numbers in this region to be artifacts. In addition, it was chosen to apply the clinical protocol for every scanner individually to demonstrate the difference that would occur in a real treatment scenario. Evaluations (data not shown) have been performed to test the differences in parameters between scanners, but this resulted in minor changes whereby the variations between the scanners seen in this study were not due to differences in the slice

thickness and FoV. The quantitative MAR evaluation (figure 5) showed comparable results for HyperSight CBCT and CT, with MAR decreasing the streak artifacts in the image. Other studies tested in-house MAR algorithms based on deep learning networks for CT (Gjesteby *et al* 2019, Puvanasunthararajah *et al* 2021) and CBCT (Liao *et al* 2019) for different metal implants, showing the same increase in image similarity after applying a MAR algorithm. Compared to the two other clinical available CBCT imagers in this study, the HyperSight CBCT MAR algorithm showed superior results and even the IR in HyperSight CBCT showed better agreement with the reference image than IR in Regular CBCT and FDK in TrueBeam CBCT (figure 5).

Furthermore, the new CBCT imager enabled the use of CBCT eFoV, where many previous on-board CBCT imagers have a limited FoV size and therefore not ideal for dose calculation purposes (e.g. for large patients or off-axis positioning of the patient) (Siewerdsen and Jaffray 2001, Jin *et al* 2010, Lim *et al* 2022). This study focused on CT number and geometry accuracy in the region outside the sFoV for HyperSight CBCT and CT. The results of HyperSight CBCT showed good overlap (Jaccard Conformity Index) for geometric accuracy, and values that were comparable to previously reported deep learning eFoV methods for CT scanners (Fonseca *et al* 2021). The geometry accuracy for the HyperSight CBCT demonstrated a higher Jaccard Conformity Index (figure 6(C)) than CT for similar phantom volumes outside the sFoV, but a lower accuracy in the CT numbers for the tissue-equivalent inserts located outside the sFoV. These larger differences in CT numbers were also found in the phantom itself (not the tissue-equivalent inserts) for the HyperSight CBCT and therefore to retrieve the correct mask, proper thresholding (−600 HU) was needed.

The phantom size dependency of CT numbers was evaluated within the sFoV with various tissue-equivalent inserts in the center of three HDPE phantoms. It was chosen to demonstrate the differences in CT numbers rather than in relative electron densities, to show the differences without variations due to the conversion curves. The CT scans were acquired at 120 kVp, while image acquisition for HyperSight CBCT was performed at 125 kVp. Ideally identical tube voltages and filters were preferred for comparability between the CT and HyperSight CBCT. However, 125 kVp was the only available setting in the current protocol of the HyperSight CBCT and as the CT did not offer this tube voltage, it was chosen to use 120 kVp. Therefore, different spectra were used and slightly lower CT numbers could be expected for high-density materials for the HyperSight CBCT images (different filtrations can also result in further differences, but this was not investigated in this study). Additionally, this study did not verify the photon spectra in the scanners. The HyperSight CBCT demonstrated larger differences in CT numbers between the phantom sizes than was seen for CT, but lower differences compared to Regular CBCT and TrueBeam CBCT. The CT number for water in the 20 cm phantom was within tolerance (± 5 HU) (Mutic *et al* 2003) and a CT-number-to-mass-density conversion curve could be calibrated for HyperSight CBCT in an identical approach as for CT (Schneider *et al* 1996, Peters *et al* 2023). The differences in CT numbers between phantom sizes show the importance of using dedicated conversion curves for different sizes to convert CT numbers properly to relative electron density, as this is a fundamental parameter in dose calculation. When the difference in CT numbers (and thereby relative electron density) is too high and over a certain threshold, the dose calculated for the patient can be affected (Thomas 1999, Kilby *et al* 2002, Papanikolaou *et al* 2004). As the CT numbers for the soft tissues were within ± 20 HU and the bone ± 250 HU compared to CT, this could lead eventually to CBCT-based dose calculation differences below 1% in head regions (Davis *et al* 2017) and 2% in pelvic regions (Papanikolaou *et al* 2004). In a recent study, HyperSight CBCT-based dose calculation showed differences below 1% compared to CT, which could allow for adaptive radiotherapy based directly on HyperSight CBCT images (Bogowicz *et al* 2024).

Furthermore, image quality was evaluated for the (CB)CT imagers by quantifying SD, SNR and CNR in the Triple Modality 3D Abdominal Phantom. It was chosen to acquire images with a clinical protocol, which means that the slice thickness between the scanners differed. A lower slice thickness in an identical systems would normally generate more noise in physics terms. However, HyperSight CBCT and CT demonstrated better results with lower slice thickness, which could be explained by the increased detector efficiency of the new CBCT panel. The results showed comparable image quality for the new CBCT imager and CT, with a slight increase in SNR and CNR for HyperSight CBCT. In a previous study, evaluating other (CB)CT imagers, the CNR for CT was almost 50% higher than for the CBCT imagers (Stock *et al* 2009). In contrast, this study showed mean ± SD quantification (Table S2 in Supplementary Material) in three soft tissue ROIs that was consistent between the HyperSight CBCT and CT (26 ± 9 HU and 39 ± 14 HU, respectively). Higher CT number variations were found in Regular CBCT (60 ± 16 HU) and TrueBeam CBCT (32 ± 29 HU) due to the presence of cupping artifacts in the images, also visible in the CT number line profiles (figure 8(B)). The non-uniformity or cupping in the Regular CBCT was in the expected range, as this system did not include the Acuros scatter correction, available in the HyperSight CBCT. The larger non-uniformity visible in the TrueBeam CBCT is related to the same limitation and the effect is expected to be larger because the imager has an anti-scatter grid with less scatter rejection and no IR.

Comparing the HyperSight CBCT performance to a previous ring-gantry imager (Regular CBCT) and C-arm imager (TrueBeam CBCT), a superior image quality and reduced noise in various body site regions were

demonstrated. Furthermore, this work showed for the first time the performance of hardware and software features, MAR reconstruction and eFoV in ring-gantry CBCT acquisition, which could improve on-line and off-line adaptive radiotherapy. These features could improve accuracy and decrease the need of correcting structures in the daily patient anatomy and auto-contouring could be more reliable, and this could enhance the CBCT dose calculation process. Additionally, due to the stability of the CT numbers, synthetic CTs or registration of the planning CT to the daily CBCT image would not be needed (de Jong *et al* 2021, Byrne *et al* 2022, Nelissen *et al* 2023). A limiting factor of this work is that it does not include dynamic phantoms to evaluate the rapid CBCT acquisition of 5.9 s compared to clinical routine of 60 s (C-arm linacs). To understand the complete HyperSight CBCT performance in a clinical workflow, image quality evaluation with dynamic phantoms for the rapid acquisitions would be recommended, but the static phantoms used in this work show the initial performance without motion present.

5. Conclusion

In conclusion, this study showed an increase in image quality and noise reduction for the HyperSight CBCT imager compared to previous CBCT imagers. In addition, it offered MAR and eFoV features that performed comparably to CT which creates possibilities for adaptive radiotherapy and an optimized workflow.

Acknowledgments

This work was partially financially supported by Varian Medical Systems.

Data availability statement

All data that support the findings of this study are included within the article (and any supplementary information files).

Trademark statement

VARIAN, HyperSight, Ethos and TrueBeam are trademarks of Varian Medical Systems, Inc., pending or registered U.S. Pat. & Tm. Off.

ORCID iDs

Gabriel Paiva Fonseca https://orcid.org/0000-0002-8087-1193
Vicki Trier Taasti https://orcid.org/0000-0002-4588-9769
Steven Petit https://orcid.org/0000-0001-9787-8239

References

Bogowicz M, Lustermans D, Taasti V T, Hazelaar C, Verhaegen F, Fonseca G P and Elmpt W van 2024 Evaluation of a cone-beam computed tomography system calibrated for accurate radiotherapy dose calculation *Phys. Imaging Radiat. Oncol.* **0** 100566 (http://phiro.science/article/S2405631624000368/fulltext)

Byrne M *et al* 2022 Varian ethos online adaptive radiotherapy for prostate cancer: early results of contouring accuracy, treatment plan quality, and treatment time *J. Appl. Clin. Med. Phys.* **23** e13479 (http://ncbi.nlm.nih.gov/pubmed/34846098)

Cai B, Laugeman E, Mazur T R, Park J C, Henke L E, Kim H, Hugo G D, Mutic S and Li H 2019 Characterization of a prototype rapid kilovoltage x-ray image guidance system designed for a ring shape radiation therapy unit *Med. Phys.* **46** 1355–70

Cheung J P, Shugard E, Mistry N, Pouliot J and Chen J 2019 Evaluating the impact of extended field-of-view CT reconstructions on CT values and dosimetric accuracy for radiation therapy *Med. Phys.* **46** 892–901

Davis A T, Palmer A L and Nisbet A 2017 Can CT scan protocols used for radiotherapy treatment planning be adjusted to optimize image quality and patient dose? A systematic review *Br J Radiol.* **90** 20160406

Fonseca G P, Baer-Beck M, Fournie E, Hofmann C, Rinaldi I, Ollers M C, van Elmpt W J C and Verhaegen F 2021 Evaluation of novel AI-based extended field-of-view CT reconstructions *Med. Phys.* **48** 3583–94

Gardner S J, Mao W, Liu C, Aref I, Elshaikh M, Lee J K, Pradhan D, Movsas B, Chetty I J and Siddiqui F 2019 Improvements in CBCT image quality using a novel iterative reconstruction algorithm: a clinical evaluation *Adv. Radiat. Oncol.* **4** 390–400

Gjesteby L, Shan H, Yang Q, Xi Y, Jin Y, Giantsoudi D, Paganetti H, De Man B and Wang G 2019 A dual-stream deep convolutional network for reducing metal streak artifacts in CT images *Phys. Med. Biol.* **64** 235003

Harris T C *et al* 2023 Impact of a novel multilayer imager on metal artifacts in MV-CBCT *Phys. Med. Biol.* **68** 145009

Hatton J, McCurdy B and Greer P B 2009 Cone beam computerized tomography: the effect of calibration of the hounsfield unit number to electron density on dose calculation accuracy for adaptive radiation therapy *Phys. Med. Biol.* **54** N329–46

Henke L E et al 2023 Prospective imaging comparison of anatomic delineation with rapid kV cone beam CT on a novel ring gantry radiotherapy device *Radiother. Oncol.* **178** 109428
Hofmaier J et al 2017 Multi-criterial patient positioning based on dose recalculation on scatter-corrected CBCT images *Radiother. Oncol.* **125** 464–9
Jaffray D A, Siewerdsen J H, Wong J W and Martinez A A 2002 Flat-panel cone-beam computed tomography for image-guided radiation therapy *Int. J. Radiat. Oncol. Biol. Phys.* **53** 1337–49
Jarema T and Aland T 2019 Using the iterative kV CBCT reconstruction on the Varian Halcyon linear accelerator for radiation therapy planning for pelvis patients *Phys. Med.* **68** 112–6
Jin J-Y, Ren L, Liu Q, Kim J, Wen N, Guan H, Movsas B and Chetty I J 2010 Combining scatter reduction and correction to improve image quality in cone-beam computed tomography (CBCT) *Med. Phys.* **37** 5634–44
Joemai R M S and Geleijns J 2017 Assessment of structural similarity in CT using filtered backprojection and iterative reconstruction: a phantom study with 3D printed lung vessels *Br. J. Radiol.* **90**
de Jong R, Visser J, van Wieringen N, Wiersma J, Geijsen D and Bel A 2021 Feasibility of Conebeam CT-based online adaptive radiotherapy for neoadjuvant treatment of rectal cancer *Radiother. Oncol.* **16** 1–11 (http://ncbi.nlm.nih.gov/pubmed/34301300)
Kilby W, Sage J and Rabett V 2002 Tolerance levels for quality assurance of electron density values generated from CT in radiotherapy treatment planning *Phys. Med. Biol.* **47** 1485–92
Liao H, Lin W-A, Huo Z, Vogelsang L, Sehnert W J, Zhou S K and Luo J 2019 Generative mask pyramid network for CT/CBCT metal artifact reduction with joint projection-sinogram correction *Lecture Notes in Computer Science* 11769 LNCS (*Lecture Notes in Artificial Intelligence and Lecture Notes in Bioinformatics*) pp 77–85 (http://arxiv.org/abs/1907.00294)
Lim R, Penoncello G P, Hobbis D, Harrington D P and Rong Y 2022 Technical note: Characterization of novel iterative reconstructed cone beam CT images for dose tracking and adaptive radiotherapy on L-shape linacs *Med. Phys.* **49** 7715–32
Maslowski A, Wang A, Sun M, Wareing T, Davis I and Star-Lack J 2018 Acuros CTS: a fast, linear boltzmann transport equation solver for computed tomography scatter: I. Core algorithms and validation *Med. Phys.* **45** 1899–913
Mutic S, Palta J R, Butker E K, Das I J, Huq M S, Loo L-N D, Salter B J, McCollough C H, Van Dyk J and (AAPM Radiation Therapy Committee Task Group No. 66) 2003 Quality assurance for computed-tomography simulators and the computed-tomography-simulation process: report of the AAPM radiation therapy committee task group No. 66 *Med. Phys.* **30** 2762–92
Nelissen K J et al 2023 Same-day adaptive palliative radiotherapy without prior CT simulation: early outcomes in the FAST-METS study *Radiother. Oncol.* **182** 109538
Papanikolaou N, Battista J J, Boyer A L, Kappas C, Klein E, Mackie T R, Sharpe M and Dyk J V 2004 *Tissue Inhomogeneity Corrections for Megavoltage Photon Beams* (AAPM) (https://aapm.org/pubs/reports/detail.asp?docid=86)
Peters N et al 2023 Consensus guide on CT-based prediction of stopping-power ratio using a hounsfield look-up table for proton therapy *Radiother. Oncol.* **184** 109675
Puvanasunthararajah S, Fontanarosa D, Wille M-L and Camps S M 2021 The application of metal artifact reduction methods on computed tomography scans for radiotherapy applications: a literature review *J. Appl. Clin. Med. Phys.* **22** 198–223
Real R and Vargas J M 1996 The probabilistic basis of jaccard's index of similarity *Syst. Biol.* **45** 380–5
Robar J L, Cherpak A, MacDonald R L, Yashayaeva A, McAloney D, McMaster N, Zhan K, Cwajna S, Patil N and Dahn H 2023 Novel technology allowing cone beam computed tomography in 6 seconds: a patient study of comparative image quality *Pract. Radiat. Oncol.*
Schneider U, Pedroni E and Lomax A 1996 The calibration of CT hounsfield units for radiotherapy treatment planning *Phys. Med. Biol.* **41** 111–24
Siewerdsen J H and Jaffray D A 2001 Cone-beam computed tomography with a flat-panel imager: magnitude and effects of x-ray scatter *Med. Phys.* **28** 220–31
De Smet M, Schuring D, Nijsten S and Verhaegen F 2016 Accuracy of dose calculations on kV cone beam CT images of lung cancer patients *Med. Phys.* **43** 5934–41
Stock M, Pasler M, Birkfellner W, Homolka P, Poetter R and Georg D 2009 Image quality and stability of image-guided radiotherapy (IGRT) devices: a comparative study *Radiother. Oncol.* **93** 1–7
Thomas S J 1999 Relative electron density calibration of CT scanners for radiotherapy treatment planning *Br. J. Radiol.* **72** 781–6
Wang Z, Bovik A C, Sheikh H R and Simoncelli E P 2004 Image quality assessment: from error visibility to structural similarity *IEEE Trans. Image Process.* **13** 600–12
Wang Z, Simoncelli E P and Bovik A C 2003 Multi-scale structural similarity for image quality assessment *Conf. Record of the Asilomar Conf. on Signals, Systems and Computers* **2** pp 1398–402
Washio H et al 2020 Metal artifact reduction using iterative CBCT reconstruction algorithm for head and neck radiation therapy: a phantom and clinical study *Eur. J. Radiol.* **132** 109293